Electric Fan Performance and Noise Modelling

An investigation of installation effects on the performance and the noise produced

Master's thesis in Mobility Engineering

MUHAMMAD MUSTAFA PARDESI

DEPARTMENT OF MECHANICS AND MARITIME SCIENCES

CHALMERS UNIVERSITY OF TECHNOLOGY
Goteborg, Sweden 2024
www.chalmers.se

Master's thesis 2024

Electric Fan Performance and Noise Modelling

An investigation of installation effects on the performance and the noise produced

MUHAMMAD MUSTAFA PARDESI

CHALMERS
UNIVERSITY OF TECHNOLOGY

Department of Mechanics and Maritime Sciences
Division of Fluid Dynamics
Chalmers University of Technology
Goteborg, Sweden 2024

Electric Fan Performance and Noise Modelling
An investigation of installation effects on the performance and the noise produced
MUHAMMAD MUSTAFA PARDESI

Supervisor: Sassan Etemad, Volvo Group Trucks Technology
Examiner: Niklas Andersson, Division of Fluid Dynamics

Master's Thesis 2024
Department of Mechanics and Maritime Sciences
Division of Fluid Dynamics
Chalmers University of Technology
SE-412 96 Goteborg
Telephone +46 31 772 1000

Typeset in LaTeX
Printed by Chalmers Reproservice
Goteborg, Sweden 2024

Electric Fan Performance and Noise Modelling
An investigation of installation effects on the performance and the noise produced
MUHAMMAD MUSTAFA PARDESI
Department of Mechanics and Maritime Sciences
Chalmers University of Technology

Abstract

This thesis investigates the effects of installation configurations on the performance and acoustic output of an electric fan using computational approaches. The study focuses on the aerodynamic and acoustic characteristics of axial fans installed in various configurations, including the use of cylindrical ducts and bellmouths. A CFD model was developed and validated against experimental data to assess fan performance in terms of pressure rise and sound power. Key distortion metrics, such as the Circumferential Distortion Index (CDI), were introduced to quantify non-uniformities in the pressure distribution. The study reveals that while the addition of certain components, such as bellmouths, improved the flow uniformity and reduced distortion, their impact on acoustic output was less straightforward. Additionally, an obstruction study was conducted to evaluate the effect of partial blockage on fan performance and distortion. The results provide insights into the relationship between installation effects and fan efficiency, pressure rise, and noise production, supporting potential design optimizations for fan installations in industrial applications.

Keywords: CFD, axial fans, acoustics, flow distortion, performance, CDI, MRF, Fan installation effects.

Acknowledgements

First and foremost, I would like to express my sincere gratitude to my examiner, Niklas Andersson, my supervisor, Sassan Etemad, and my co-supervisors, Mikael Karlsson and Michail Vourakis, for their invaluable guidance, support, and encouragement throughout this period. Their expertise and insightful feedback have been instrumental in shaping this thesis, and I am truly grateful for their mentorship.

I would also like to express my deepest gratitude to my family for their unwavering support, patience, and belief in me throughout my studies. In particular, I want to honor the memory of my mother, who sadly passed away during the course of this thesis. Her love and encouragement have been a constant source of strength.

A special mention to Torbjörn, whose thoughtful insights during the pre-processing stage were invaluable, and to Ashik, whose brainstorming sessions provided clarity. Your contributions have been instrumental to the successful completion of this thesis.

Thank you all for your support.

Muhammad Mustafa Pardesi, Goteborg, October 2024

List of Acronyms

Below is the list of acronyms that have been used throughout this thesis listed in alphabetical order:

AIP	Aerodynamic Interface Plane
CDI	Circumferential Distortion Index
CFD	Computational Fluid Dynamics
RDI	Radial Distortion Index

Nomenclature

Below is the nomenclature of all the symbols used throughout the thesis.

$\mathbf{g}$	Gravity vector
p	Pressure
$P_{R,avg}$	Ring average total pressure
$P_{R,min}$	Ring minimum total pressure
$P_{AIP,avg}$	Average total pressure
u	Velocity in x-direction
$\hat{u}$	specific internal energy
u_t	Friction velocity
u^+	Dimensionless velocity
$\mathbf{V}$	Velocity vector
y^+	Dimensionless wall distance
y	Distance to nearest wall

Greek Symbols

κ	Von Karman constant
ρ	Density
μ	Dynamic viscosity
ϕ	Viscous dissipation function
τ_w	Wall shear stress

Mathematical Symbols

∇	Nabla operator

Contents

List of Figures

List of Tables

1

Introduction

1.1 Background

Electric fans, commonly referred to as e-fans, are becoming increasingly vital in the thermal management systems of next generation vehicles, such as battery electric vehicles (BEVs) and fuel cell electric vehicles (FCEVs). These fans are integral not only during typical driving conditions but also during periods of charging, particularly fast charging, when thermal loads are heightened. As the battery or fuel cell systems operate, they generate significant heat that must be efficiently dissipated to prevent damage and maintain performance. E-fans help by creating the necessary airflow to cool critical components like the battery packs, inverters, and electric motors through forced convection.

In conventional combustion engine vehicles, much of the noise generated is masked by the engine itself, leaving little attention paid to auxiliary noise sources such as cooling fans. However, in electric vehicles (EVs), the absence of noisy internal combustion engines makes previously minor noises, like those from e-fans, far more noticeable to both passengers and pedestrians. This increase in fan audibility is becoming a significant issue, as the sound emitted during fan operation can affect the comfort of vehicle occupants and contribute to overall noise pollution, especially in urban environments.

In response, new and more stringent noise regulations are being introduced, which electric vehicles must adhere to. These regulations are designed to minimize the overall acoustic footprint of EVs, particularly during fan operation. As a result, automakers and engineers are focusing not only on the efficiency of e-fans for thermal management but also on reducing their noise output. This challenge requires innovations in fan design, such as improved blade geometry, better material choices, and more advanced motor control techniques, to strike a balance between performance and noise reduction. This growing demand underscores the importance of quieter, more efficient e-fans in the design of future BEVs and FCEVs.

This thesis investigates the effects of installation configurations on the performance and acoustic output of an electric fan using computational approaches. The study focuses on the aerodynamic and acoustic characteristics of axial fans installed in various configurations, including the use of cylindrical ducts and bellmouths. A CFD model was developed and validated against experimental data to assess fan

performance in terms of pressure rise and sound power. Key distortion metrics, such as the Circumferential Distortion Index (CDI), were introduced to quantify non-uniformities in the pressure distribution. The study reveals that while the addition of certain components, such as bellmouths, improved the flow uniformity and reduced distortion, their impact on acoustic output was less straightforward. Additionally, an obstruction study was conducted to evaluate the effect of partial blockage on fan performance and distortion. The results provide insights into the relationship between installation effects and fan efficiency, pressure rise, and noise production, offering potential design optimizations for fan installations in industrial applications.

2

Theory

This section provides the essential theoretical background for the thesis. It includes the principles of fluid mechanics and their application in Computational Fluid Dynamics (CFD), as well as the fan theory, which elucidates the underlying physics of axial fans.

2.1 Fundamentals Of Fluid Mechanics

2.1.1 Governing equations

The equations governing fluid motion encompass the conservation laws for mass, momentum, and energy, are shown in equations 2.1, 2.2, and 2.3 respectively. The mass conservation principle asserts that the mass entering a control volume is exactly equal to the mass exiting it, ensuring that mass is neither created nor destroyed within the control volume. This is fundamental for maintaining the consistency of fluid flow. The momentum conservation principle, derived from Newton's second law of motion, describes how fluid particles' velocity changes under the influence of various forces. It ensures that the forces acting on the fluid, including pressure, viscous, and external forces, are in equilibrium with the fluid's motion and is crucial for predicting how fluids move and interact with their surroundings. The energy conservation law states that the total energy within a control volume remains constant, accounting for internal energy, work done by fluid forces, and heat transfer. It ensures that energy changes within the control volume are balanced by the energy added or removed through heat, work, and mass flow. It is essential for understanding the thermal dynamics and energy exchanges in fluid systems. [1]

$$\frac{\partial \rho}{\partial t} + \nabla \cdot (\rho \mathbf{V}) = 0 \tag{2.1}$$

$$\rho \frac{D\mathbf{V}}{Dt} + \nabla p = \mu \nabla^2 \mathbf{V} + \rho \mathbf{g} \tag{2.2}$$

$$\rho \frac{D\hat{\mathrm{u}}}{Dt} + p(\nabla \cdot \mathbf{V}) = \nabla \cdot (k \nabla T) + \Phi \tag{2.3}$$

2.1.2 Turbulent boundary layer

This study involves flow with a high Reynolds number, that is to say, the flow is turbulent. In order to accurately predict the flow, it is important to accurately predict

the flow in the boundary layer region where the viscous forces are not negligible. The boundary layer is defined as the layer near the wall up to the point where the flow velocity reaches 99% of the free stream velocity. When mathematically defining the boundary layer, it can be split into the inner and outer layers. Turbulent effects dominate in the outer layer whereas the inner layer can further be divided into three sub-layers, each having different flow characteristics:

- **Viscous Sub-layer**
  This is the layer closest to the wall and is dominated by viscous effects and the flow is nearly laminar. The mean flow velocity in this region is determined by fluid density, viscosity, distance from the wall, and wall shear stress.
- **Log Layer**
  It is the layer furthest from the wall and is dominated by turbulent effects.
- **Buffer Layer**
  This is the transitional layer between the *viscous sub-layer* and the *log layer*.

The velocity profile for the turbulent boundary layer with its different layers and sub-layers is shown in figure 2.1 below. [2]

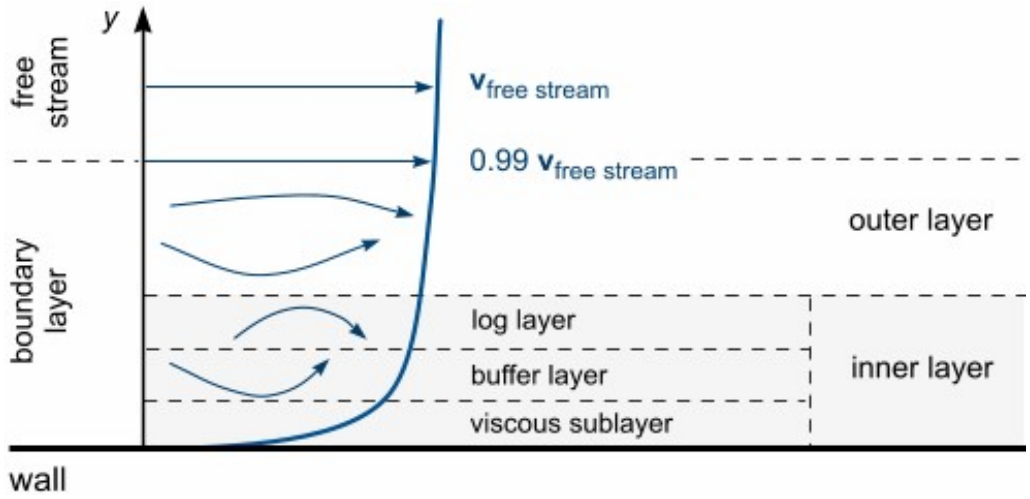

Figure 2.1: Velocity profile of a turbulent flow

In the viscous sub-layer,

$$y^+ < 5 \qquad\qquad y^+ \approx u^+$$

In the log layer, for $y^+ > 30$, the log law

$$u^+ = \frac{1}{\kappa} \ln y^+ + B$$

can be used to approximate the dimensionless velocity, where the dimensionless values are defined as

$$y^+ = \frac{y u_t}{v} \qquad\qquad u_t = \sqrt{\frac{\tau_w}{\rho}} \qquad\qquad u^+ = \frac{u}{u_t}$$

The values of the constants, κ and B, are obtained from experiments for a smooth wall. [3]

However, in the buffer layer, between the viscous sub-layer and the log layer where $5 < y^+ < 30$, neither of the equations yields accurate results

Figure 2.2 below shows the boundary layer behavior.

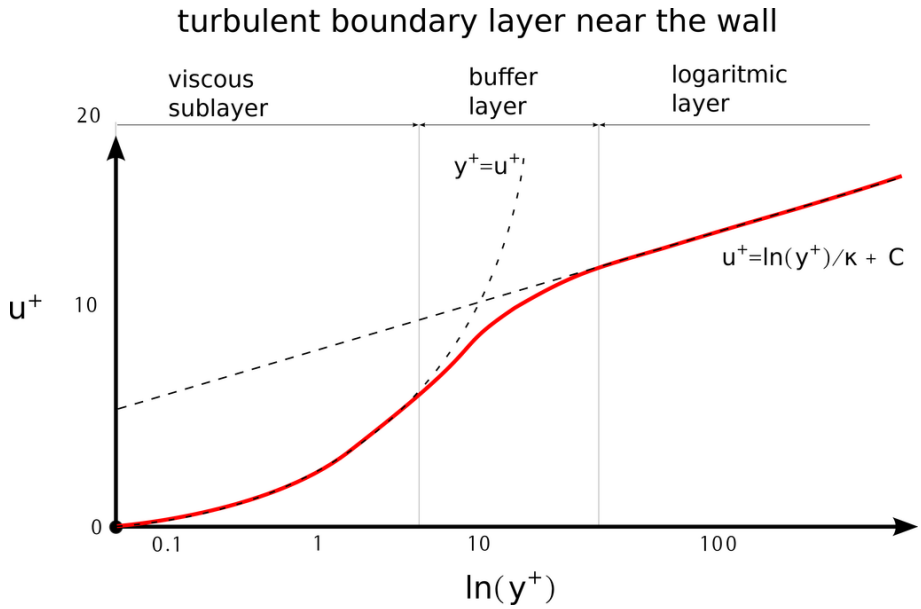

Figure 2.2: Graph showing relation between y^+ and u^+ in the boundary layer

2.2 Computational Fluid Dynamics

2.2.1 Turbulence modelling

The flow being studied has a high Reynolds number, which means it is turbulent and requires a suitable turbulence model for proper analysis. After trying out different models in STAR-CCM+, it was found that the Spalart-Allmaras model with low-y^+ wall treatment worked best. It gave the most accurate results when compared to the experimental data.

2.2.2 Moving Reference Frame

Since this study involves a rotating fan, a moving reference frame is used to model the rotating motion of the fan. Moving reference frame allows the rotational flow to be solved in steady-state giving a time-averaged behavior of the flow which serves as a compromise between accuracy and computational time. It is solved by keeping the rotating parts stationary while numerically incorporating the rotating effects in the source terms. [4]

2.3 Fan Acoustics

In axial fans, sound is emitted primarily by mechanisms governing sound generation of airfoils and by the rotating motion of the fan blades.

2.3.1 Sound generation mechanisms for airfoils

In subsonic flow, which is the case of our project, sound is generated from an airfoil due to two mechanisms:

- airfoil self-noise
- turbulence ingestion noise (also known as leading edge noise)

These mechanisms are similar for the fan blades.[5]

2.3.1.1 Airfoil Self-noise

Airfoil self-noise is the sound generated by an airfoil operating under uniform and non-turbulent inflow conditions regardless of whether the airfoil is moving in an air stream or a stationary medium. It consists of *boundary layer noise, boundary layer separation noise, trailing edge noise*, and *tip noise*.

Boundary Layer Noise: It is generated due to the pressure fluctuations under a turbulent boundary layer. It is broadband in nature and radiates from the middle part of the airfoil.

Boundary Layer Separation Noise: It is generated under stall conditions, that is, when the flow is separating from some part of the airfoil. The major source is the complex flow field that develops around the airfoil due to the flow separation. The sound is radiated from the trailing edge if the flow is lightly separated; otherwise, it is radiated along the entire chord if the airfoil stalls or is in the deep stall region.

Trailing Edge Noise: It depends on the boundary layer. If the boundary layer is laminar on at least one side of the airfoil, vortex shedding can occur resulting in a noise with tonal characteristics and directly linked to the vortex shedding frequency. On the other hand, if the boundary layer is turbulent, eddies are convected past the trailing edge. Boundary layer parameters and trailing edge thickness determine the vorticity and the vortex shedding frequency. The noise produced has broadband characteristics in general but can be tonal if the trailing edge is sharp. If the trailing edge is blunt, vortex shedding occurs, similar to the Von Karman vortex. The noise produced is of dipole type and therefore has tonal characteristics for both turbulent and laminar flow regimes. Vortex shedding frequency depends on the trailing edge thickness.

Tip Noise: It is generated when the airfoil is attached on one end so on the free end, a cross flow occurs from the pressure side to the suction side resulting in tip vortices that produce noise similar to the trailing edge. The noise produced is broadband in nature.[5]

2.3.1.2 Turbulence ingestion noise

For the generation turbulence ingestion noise, also known as leading-edge noise, there are two cases that depend on the turbulence parameters, particularly on the integral length scale, Λ, which measures the extent of the region over which the velocities are correlated, that is, the size of large eddies.[6]

If the integral length scale of the inflow is larger than the chord length, a total pulsating airfoil loading is induced on the airfoil. The noise produced is of broadband type and contributes to the lower frequencies in the spectrum. The wavelength is greater than the chord length and therefore the source can be regarded as acoustically compact and hence the sources cannot be assigned to any particular region.

On the other hand, if the integral length scale of the inflow is smaller than the chord length, pressure fluctuations develop on the leading edge in a localized manner. The noise generated is of broadband type and contributes to the higher frequencies in the spectrum. The airfoil is no longer acoustically compact and noise sources can be assigned to the leading edge.[5]

2.3.2 Sound generation due to rotation of the fan

In addition to the sound generation due to mechanisms for airfoil, which are similar for the fan blades, noise is also generated due to mechanisms owing to the rotational motion of the fan blades. These are:

- rotor self-noise,
- turbulence ingestion noise (also known as leading edge noise),
- unsteady loading noise,
- sub-harmonic tip noise, and
- rotating stall.

2.3.2.1 Rotor self-noise

This includes the airfoil self-noise discussed earlier and in addition to this, due to the rotational motion of the fan blade, it includes additional sound sources known as *thickness noise* and *steady loading noise*.

Thickness noise: This noise is generated due to the fluid of finite thickness being displaced by the rotation of the fan blade. It has tonal characteristics and the contribution to the overall noise is negligible.

Steady loading noise: This noise is generated due to the lift force produced by the fan blade under steady conditions. It is only audible in the stationary frame of reference where it is observed as harmonic pressure changes and therefore the noise has tonal characteristics and is emitted at the blade passing frequency. The contribution to the overall noise is negligible.[5]

2.3.2.2 Turbulence ingestion noise

This includes the same mechanisms for airfoil turbulence ingestion noise discussed earlier.

2.3.2.3 Unsteady loading noise

This is generated due to unsteady temporal fluctuations, blade forces, etc. Similar to the steady loading noise, it is observed in a stationary frame of reference as harmonic pressure fluctuations induced by rotating unsteady pressure fields. The noise generally has tonal characteristics and is emitted at the blade passing frequency. It includes the following mechanisms which lead to unsteady blade forces:

Ingested turbulence: It is generated due to turbulent inflow conditions which change the blade loading. The noise has both tonal and broadband characteristics.

Spatially inhomogeneous inflow conditions: Due to the inhomogeneous inflow conditions, the fan blades experience fluctuating flow velocities leading to change in the angle of attack resulting in unsteady blade loading.

Rotor stator interactions: Due to the interactions between the wakes formed downstream of the fan and the stator vanes, a pressure pulse is generated every time the angular position of the fan blade coincides with the stator vane. The sound generated has tonal characteristics. It increases with increasing angular velocity and with decreasing distance between the stator and the rotor.[5]

2.3.2.4 Sub-harmonic tip noise

Sub-harmonic tip noise is generated in addition to the tip noise from the rotor-self noise and depends on the fan blade geometry and the operating point.[5]

2.3.2.5 Rotating Stall

Rotating stall is produced as a narrow band noise due to flow separation in the blade channels if the axial fan is performing in the deep stall region.[5]

3
Methods

In this chapter, the methods used to conduct the study are presented. It includes a detailed description of the geometry of the fan and the test rig, the generated mesh used in the numerical simulations, the validation process of the simulation model, and finally, the presentation of the different cases studied in this project.

3.1 Methodology and Limitations

The thesis began with an extensive literature review to understand the physics behind noise generation in low-pressure axial fans and explore the relevant installation cases to this study. This phase was particularly challenging, as the concepts were more advanced than I had previously encountered, requiring substantial reading and research. Additionally, while I had previous experience with CFD simulations, learning to simulate rotational motion was a rewarding challenge and a great learning opportunity that expanded my skills. A significant limitation of the thesis arose when the planned experimental testing was canceled, forcing me to rely on previously collected experimental data. This data was limited and lacked uncertainty measurements, making it difficult to interpret the results and draw definitive conclusions.

3.2 Experimental setup

The experimental testing of the fan was initially planned to be conducted at Volvo GTT's fan test rig. However, due to time constraints, it was canceled. Instead, previously available experimental data for the same fan will be used to validate the model. The experiment consists of four different installation cases, shown in figure 3.1.

(a) Case A: Fan with shroud

(b) Case B: Fan with shroud and cylindrical duct

(c) Case C: Fan with shroud and bell-mouth

(d) Case D: Fan with shroud, cylindrical duct, and bell-mouth

Figure 3.1: Installation cases

The previous experiment consisted of two parts. The first part involved recording the rise in pressure for eight volume flow rates from 0.3-1.0 m^3/s to produce a fan curve for each case. The fan curve for the installation case A was used to validate the simulation model. The second part involved recording noise levels using a grid of microphones for each of the four cases, focusing on two volume flow rates. The experiment was carried out at 4100 rpm. The experimental results for each case from both parts are presented below in the figures 3.2-3.5.

Case A	
Volume flow rate, m^3/s	**Pressure, Pa**
0.33	473.60
0.40	433.14
0.51	446.40
0.60	411.02
0.70	339.05
0.80	243.56
0.90	122.92
1.00	3.35

(a) Experimental data for Case A

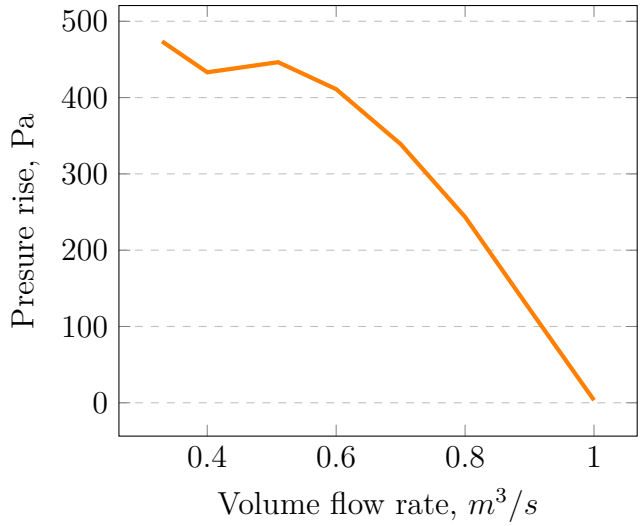

(b) Fan Curve for Case A

Case A		
Volume flow rate, m^3/s	**Pressure, Pa**	**Total sound power, 10^{-3} dB**
0.59	415.17	9.04
0.90	129.99	8.93

(c) Acoustic data for Case A

Figure 3.2: Experimental results for Case A

Case B	
Volume flow rate, m^3/s	**Pressure, Pa**
0.33	507.86
0.41	483.30
0.50	459.52
0.60	422.25
0.70	355.08
0.81	253.87
0.90	140.72
1.00	21.59

(a) Experimental data for Case B

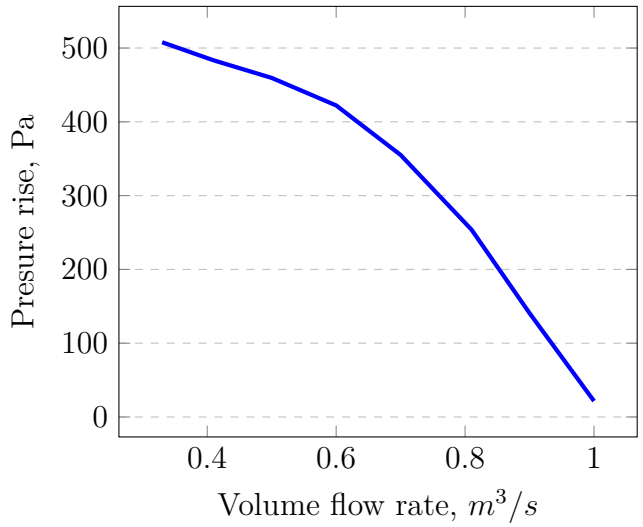

(b) Fan Curve for Case B

Case B		
Volume flow rate, m^3/s	**Pressure, Pa**	**Total sound power, 10^{-3} dB**
0.59	429.30	9.14
0.90	147.31	9.25

(c) Acoustic data for Case B

Figure 3.3: Experimental results for Case B

Case C	
Volume flow rate, m^3/s	**Pressure, Pa**
0.34	539.57
0.42	483.26
0.51	460.55
0.60	429.39
0.71	353.23
0.80	260.63
0.90	151.33
1.00	33.28

(a) Experimental data for Case C

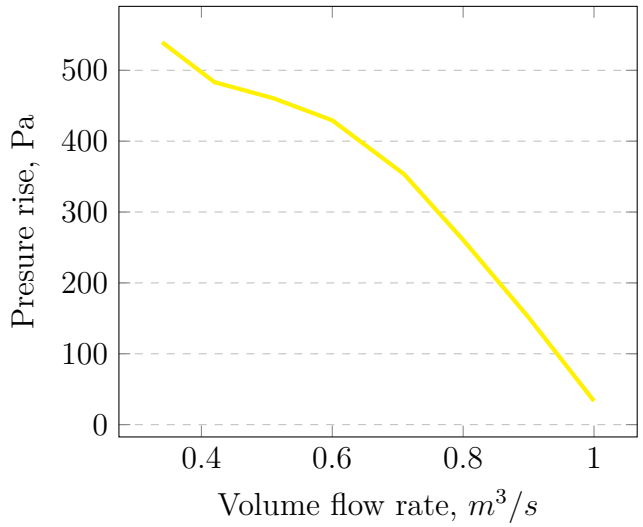

(b) Fan Curve for Case C

,

Case C		
Volume flow rate, m^3/s	**Pressure, Pa**	**Total sound power, 10^{-3} dB**
0.59	435.06	9.36
0.90	168.77	8.97

(c) Acoustic data for Case C

Figure 3.4: Experimental results for Case C

Case D	
Volume flow rate, m^3/s	**Pressure, Pa**
0.33	521.80
0.42	485.17
0.51	464.94
0.60	430.50
0.71	351.57
0.80	262.94
0.91	148.79
1.00	74.54

(a) Experimental data for Case D

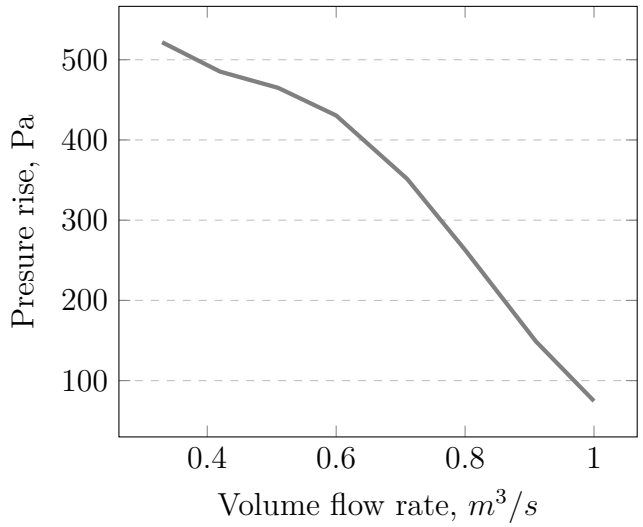

(b) Fan Curve for Case D

Case D		
Volume flow rate, m^3/s	**Pressure, Pa**	**Total sound power, 10^{-3} dB**
0.59	434.71	9.39
0.90	167.48	8.91

(c) Acoustic data for Case D

Figure 3.5: Experimental results for Case D

3.3 Simulation Model Setup

For the simulation, the CAD model of the fan test rig including the fan, provided by Volvo GTT, was used. Since the simulation consists of rotating and stationary parts, it was decided to divide the geometry into stationary and rotating regions with interfaces between them.

3.3.1 Geometry

The geometry consists of two main parts:

- Fan test rig
- Fan region

3.3.1.1 Fan test rig

The fan test rig geometry is based on the CAD model of the actual test rig where fan testing is conducted. This test rig replicates the environmental conditions that the fan experiences in a truck, ensuring realistic results.

It consists of three main parts:

- The **inlet chamber** houses the equipment that produces the desired ram air flow for the experiment. It also has sensors to record the inlet pressure.
- The **wall** between the inlet and outlet chambers holds the fan assembly, ensuring that air passes exclusively through the fan.
- The **outlet chamber** records the outflow parameters from the fan. It is also equipped with a microphone grid to capture the acoustic output of the fan's outlet flow but is not included in the geometry as the acoustic testing was not part of the project.

For simplicity, the model does not include the equipment, used for producing the ram air flow as those are of no interest. Instead, the wall, shown in figure 3.6 in red, is set as a *mass flow inlet boundary*. Since the flow velocity is not greater than 0.3 Ma, the flow is modeled as incompressible and therefore the density remains constant so the inlet mass flow depends only on the volume flow rate which is parameterized in the simulation. The direction of the air flow is perpendicular to the wall.

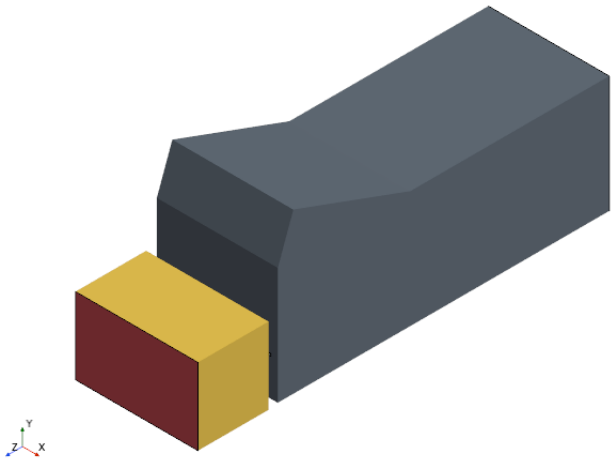

Figure 3.6: View of the rig showing inlet boundary

The outlet wall, shown in figure 3.7 in pink, is set as *pressure outlet boundary*. The rest of the walls of the fan test rig are set as *wall boundaries*.

Figure 3.7: View of the rig showing outlet boundary

3.3.1.2 Fan geometry

The fan geometry is also based on the CAD model of the actual fan which is prepared and provided by Volvo GTT. It consists of the fan rotor, stator, and the different installations used for the study in this thesis. Only the installations are shown in figure 3.8. The fan and the rotor are not shown due to confidentiality restrictions from Volvo GTT.

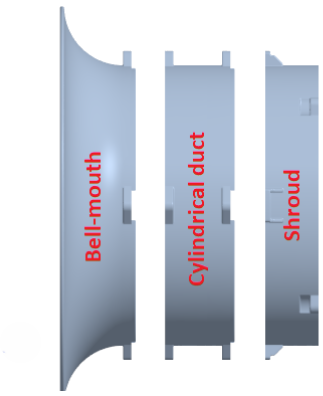

Figure 3.8: Installations for the fan geometry

3.3.1.3 Fluid domain

Since the fan rotates relative to the fan test rig, dividing the fluid domain into stationary and rotating regions is more effective.

The stationary region includes all the non-moving parts, such as the fan test rig, installations, and stator. The rotating region is defined by a set of boundaries that enclose the fan, some of which serve as interfaces between the stationary and rotating regions. To simulate the fan's rotation, a rotating reference frame is created and applied to the rotating region. The rotational speed is set to match the testing conditions, i.e., **4100 rpm**.

The fluid flow is modeled using the *Spallart-Allmaras* turbulence model with Low-y^+ wall treatment, as it is considered robust for modeling aerodynamic applications [7] and showed better results compared to other turbulence models. The constant density model is used to model the behavior of air with the density value being set at $\mathbf{1.167\ kg/m^3}$ from the experimental setup The reference pressure is set to **101325 Pa**.

3.3.2 Mesh generation and dependence study

Polyhedral cells are used for meshing the fluid region. Since the area close to the fan is of primary interest, the cells near the fan are refined, while the cells in other areas are coarser to limit the total number of cells and reduce computational power requirements. Prism layers are applied only on the fan, stator, and installation fan surfaces to resolve the boundary layers accurately. The prism layers are set to a total of 10 layers with the total thickness of the prism layer being 1.9 mm. Figure 3.9 shows the mesh of the region close to the fan.

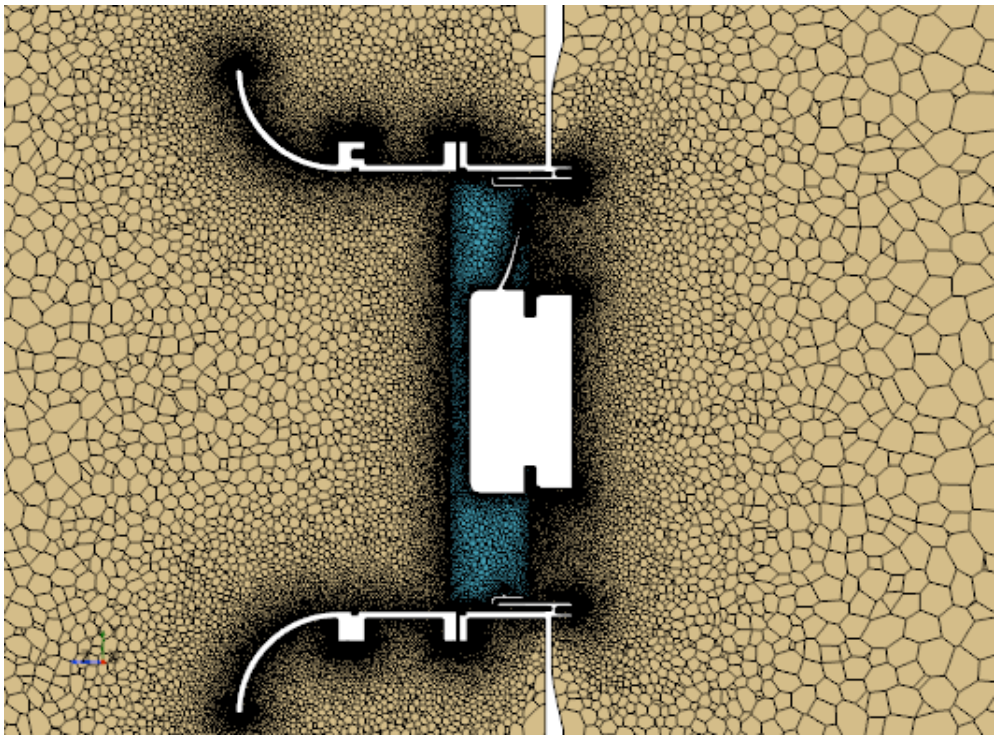

Figure 3.9: Mesh for region close to fan

For the mesh dependence study, three different mesh sizes were chosen for the fan geometry and the model for case A was run at the most efficient operating point i.e. 0.6 m^3/s. This was done to see how sensitive the solution is to mesh refinement. Table 3.1 below shows the parameters for different cases.

Case	**Cell size**	**Cell count**	**1st layer cell height corresponding to y^+**
Case 1	1 mm	10.5 million	0.1
Case 2	2 mm	7.04 million	0.1
Case 3	3 mm	6.33 million	0.1

Table 3.1: Cases for mesh dependence study

3.3.3 Validation of the CFD model

Before running the CFD model for further studies, it is necessary to validate the CFD model using the experimental measurements. For validation, the model for case A is used, and the simulations are run for the operating range of the fan curve which is from $0.6 - 0.9$ m^3/s. Inlet and outlet pressures from the simulation are recorded at the same locations as in the experiments.

3.3.4 Further studies

After validating the model, all cases are simulated to identify any correlations between the acoustic output and flow field parameters. This analysis is then used for a case study, where the model for case D is simulated with an obstruction grill shown in figure 3.10. The results are compared to the existing model of case D, and predictions are made regarding the acoustic output for these scenarios.

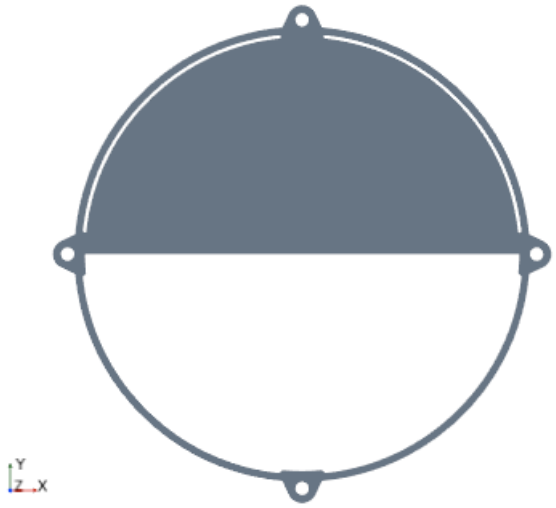

Figure 3.10: Half-moon obstruction

4

Results

This chapter presents the simulation results in the form of tables and plots.

4.1 Mesh dependence study

As outlined in section 3.3.2, the mesh study involved running simulations for three different mesh sizes at an operating point of 0.6 m^3/s. The varying mesh sizes were applied specifically to the regions near the fan, while the rest of the rig maintained a consistent mesh size. The mesh that produced a pressure rise closest to the experimental value was selected for further use.

Case	**Cell size**	**Simulation result**	**Experimental result**	**error**
Case 1	1 mm	371.96 Pa	411.02 Pa	9.5 %
Case 2	2 mm	315.63 Pa	411.02 Pa	23.2 %
Case 3	3 mm	316.89 Pa	411.02 Pa	22.9 %

Table 4.1: Mesh dependence study results

Table 4.1 shows that the finest mesh size, 1 mm, yields the most accurate results and will therefore be used for all subsequent studies. While a finer mesh could potentially offer even better accuracy, the significantly increased computational time made it impractical to pursue.

4.2 CFD model validation

As noted in section 3.3.3, it is essential to validate the model using experimental data before proceeding with further studies. The mesh size selected from the mesh dependence study was used for this validation. Although the experiments covered operating points from $0.3 - 1.0$ m^3/s, the validation was conducted for a range of $0.6 - 0.9$ m^3/s. This range was chosen because, for flows below 0.6 m^3/s, the fan operated in the stall region, and for flows above 0.9 m^3/s, the simulation showed airflow reversal, meaning the fan produced a negative pressure rise. The results of the validation are shown in table 4.2 below.

Operating point	Experimental result	Simulation result	error
0.6 m^3/s	411.02 Pa	371.96 Pa	9.5 %
0.7 m^3/s	339.05 Pa	305.92 Pa	9.77 %
0.8 m^3/s	243.56 Pa	214.59 Pa	11.89 %
0.9 m^3/s	122.92 Pa	97.23 Pa	20.9 %

Table 4.2: CFD model validation results

The study results show that the simulation error is under 12% for all operating points, except for $0.9m^3/s$, which has an error of approximately 21%. With an average error of 13%, the model can be considered validated. One possible source of error could be inaccuracies in the experimental data, as the uncertainties associated with the experimental measurements were not provided.

4.3 Acoustic study

Following the validation of the CFD model, the next and most critical objective of this thesis is to determine whether any correlation exists between the fan's total sound power and the flow parameters. Before delving into this analysis, it is essential to introduce two key parameters relevant to the study: the *Circumferential Distortion Index (CDI)* and the *Radial Distortion Index (RDI).*

4.3.1 CDI and RDI

The *Circumferential Distortion Index* (CDI) and *Radial Distortion Index* (RDI) are two of the most commonly used descriptors for assessing distortion. Both indices provide insight into the non-uniformity of the total pressure distribution over a plane upstream of the fan, known as the Aerodynamic Interface Plane (*AIP*). The *AIP* is perpendicular to the flow direction. While both indices measure pressure distortion, CDI focuses on circumferential distortion, and RDI measures radial distortion, as their names suggest.[8]

To calculate the *Circumferential Distortion Index* (CDI), the *AIP* is divided into multiple circumferential rings, and CDI is calculated for each ring. The final CDI is determined by taking the maximum of the averages of two consecutive rings. The equation below illustrates the calculation of CDI.

$$CDI = \max\left(\frac{\mathrm{CDI}_i + \mathrm{CDI}_{i+1}}{2}\right)$$

Where the CDI_i is defined at each ring and is the difference between the ring average total pressure and the ring minimum total pressure relative to the *AIP* total average pressure.[8]

$$\mathrm{CDI}_i = \frac{P_{R,avg} - P_{R,min}}{P_{AIP,avg}}$$

Similarly, the *Radial Distortion Index* is calculated by taking the maximum value from the radial distortion at the inner and the outer radii while the RDI_i, defined at each ring, is the difference between the ring average total pressure and the *AIP* average total pressure relative to the AIP average total pressure. Due to its similarity with the *CDI*, it will not be used for this study. The equations below show the calculation of the *RDI*.[8]

$$RDI = \max\left(\mathrm{RDI}_{inner}, \mathrm{RDI}_{outer}\right)$$

$$\mathrm{RDI}_i = \frac{P_{AIP,avg} - (P_{R,avg})_i}{P_{AIP,avg}}$$

4.3.2 Results

In this section, the results of the study involving the installation cases will be presented. As outlined in section 3.2, the acoustic experiment was only conducted at two operating points, 0.6 m^3/s and 0.9 m^3/s, for all the original cases. *CDI* and efficiency were calculated for all the cases. It is important to note that the efficiency discussed here refers to aerodynamic efficiency, derived from the simulation data. Determining the actual or total efficiency was not possible due to the lack of comprehensive experimental data. For reference, readers may wish to consult figure 3.1 to recall the specific cases discussed in this section. Table 4.3 presents the findings of the study.

Operating point: 0.6 m^3/s

Case	**Experiment ΔP, Pa**	**Total Sound Power , 10^{-3} dB**	**Simulation ΔP, Pa**	**Efficiency, %**	**CDI, 10^{-6}**
A	411.02	9.04	371.96	54.86	1.38
B	422.25	9.14	379.53	51.77	1890
C	429.39	9.36	386.15	55.45	94.8
D	430.50	9.39	389.29	55.20	760

(a) Results for 0.6 m^3/s

Operating point: 0.9 m^3/s					
Case	**Experiment ΔP, Pa**	**Total Sound Power , 10^{-3} dB**	**Simulation ΔP, Pa**	**Efficiency, %**	**CDI, 10^{-6}**
A	122.92	8.93	97.23	15.77	1.40
B	140.72	9.25	136.22	30.75	838
C	151.33	8.97	113.65	27.36	20.7
D	148.79	8.91	121.47	29.17	87.6

(b) Results for 0.9 m^3/s

Table 4.3: Results for acoustic study

Pressure rise

The results from table 4.3 indicate a consistent increase in pressure rise by the fan from case A to case D. This trend is evident in both the simulation and experimental results for the operating point of 0.6 m^3/s. However, at the operating point of 0.9 m^3/s, the increase is observed only in the experimental results. The simulation results generally follow an upward trend but show a notable discrepancy in case B, where the error is significantly lower compared to the other cases.

As shown in Table 4.2, the error at the operating point of 0.6 m^3/s is approximately 10%, while at 0.9 m^3/s, it is around 21%. For the 0.6 m^3/s operating point, all simulation cases have an error of about 10%. However, at 0.9 m^3/s, the error remains around 21% for all cases except for case B, which has an unusually low error of 3%. Adjusting the error for case B to align with the other cases would result in a corrected value of 111.17 Pa, down from 136.22 Pa, thereby making the trend consistent with that observed at the 0.6 m^3/s operating point. This is shown in the graph in the figure below. It is important to note that for all cases, the volume flow rate and rotational speed remain constant. Therefore, the observed increase in pressure rise can be attributed solely to the addition of the cylindrical duct and the bell-mouth, which also contributes to the increased total sound power.

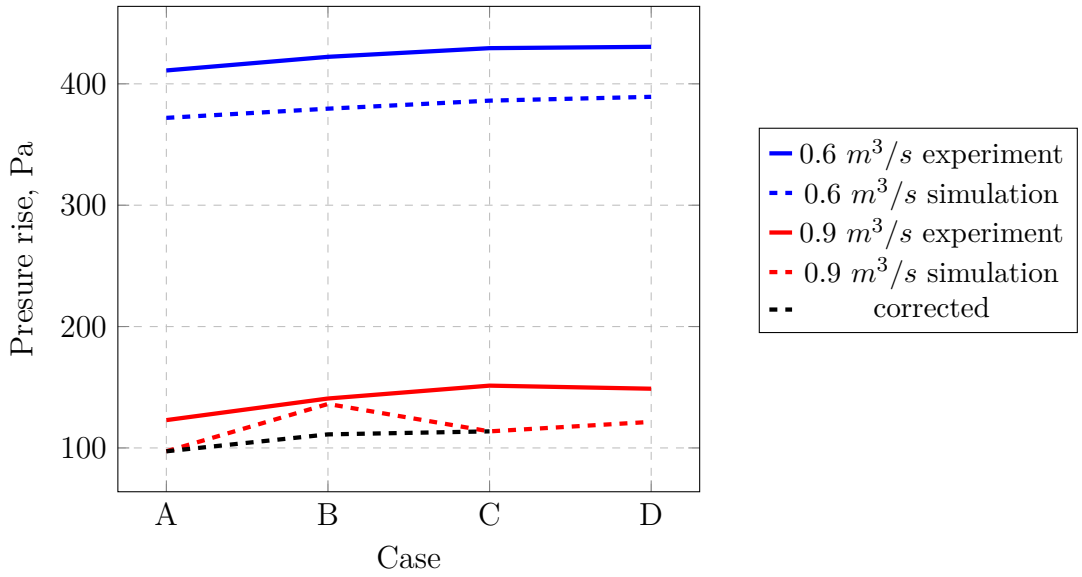

Figure 4.1: Comparison of experimental and simulation pressure rise

Acoustic output

From Table 4.3, it can be observed that for the operating point of 0.6 m^3/s, the total sound power consistently increases across the cases. However, for the operating point of 0.9 m^3/s, the total sound power increases from case A to case B but then shows a decreasing trend. Generally, the total sound power is higher for the operating point of 0.6 m^3/s than for 0.9 m^3/s, except for case B, which has a significantly higher output compared to other cases. This discrepancy could be due to uncertainties in the total sound power readings, which are not known.

Considering the trend for the operating point of 0.6 m^3/s, it can be inferred that from case A to D, corresponding to an increase in pressure rise, the total sound power also increases. However, this trend does not hold for the operating point of 0.9 m^3/s, making it inconclusive whether a clear correlation exists between pressure rise and total sound power. Therefore, more experimental data are required to determine if such a correlation exists. One thing is conclusive from these results: a higher pressure rise generally leads to higher total sound power.

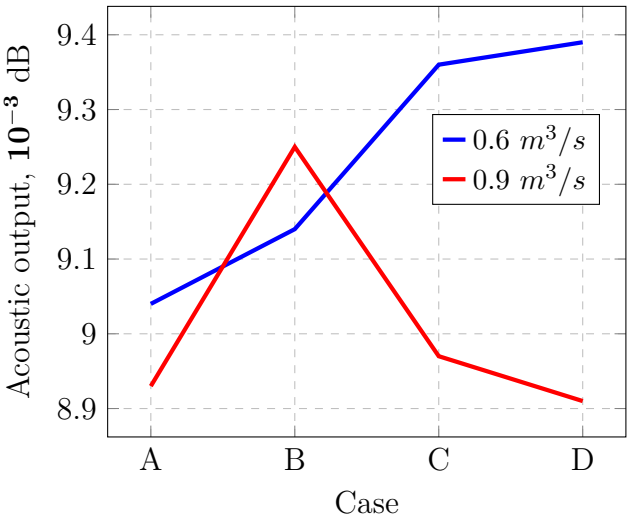

Figure 4.2: Comparison of total sound power

Circumferential Distortion Index

From Table 4.3, it can be observed that both operating points follow a similar trend in *CDI*. The *CDI* reaches its peak in case B, decreases in case C, and then rises again in case D. The data indicates that a higher pressure rise generally corresponds to a higher *CDI*. Furthermore, the addition of the bellmouth appears to reduce the *CDI*, as demonstrated by the lower values in case D compared to case B. This reduction is likely due to the bellmouth's ability to smooth the airflow, in contrast to the cylindrical duct, which tends to cause flow stagnation at the duct edges, leading to greater distortion. Figure 4.4 illustrates the total pressure distribution on the *AIP* for case B, showing noticeable distortion around the edges. In contrast, figures 4.3, 4.5, and 4.6, which display the total pressure distribution for cases A, C, and D respectively, reveal a more uniform spread of total pressure, resulting in comparatively lower distortion.

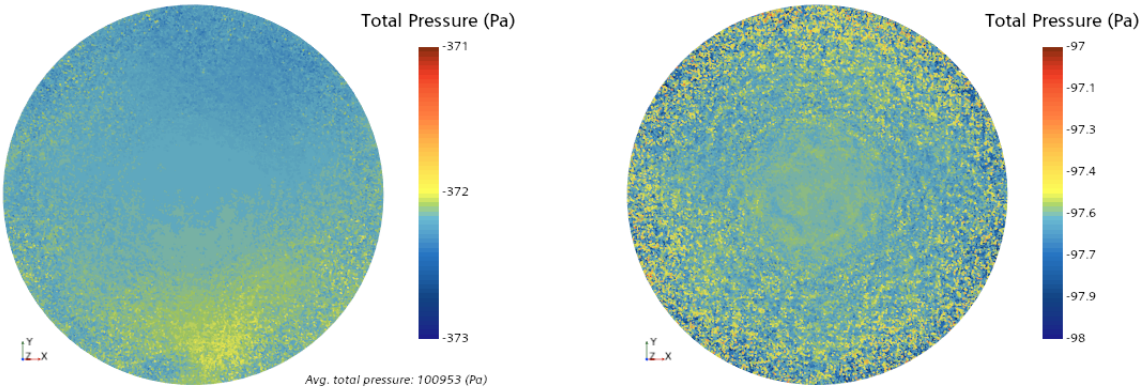

(a) 0.6 m^3/s **(b)** 0.9 m^3/s

Figure 4.3: *AIP* total pressure for case A

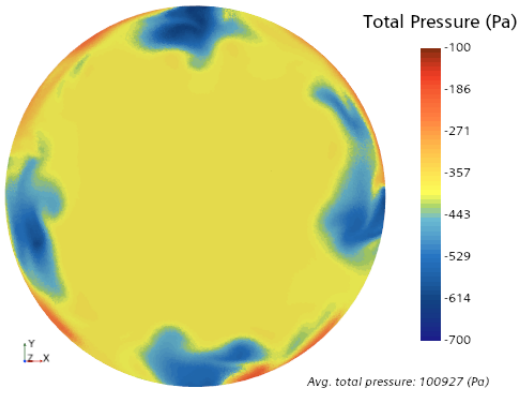

(a) 0.6 m^3/s

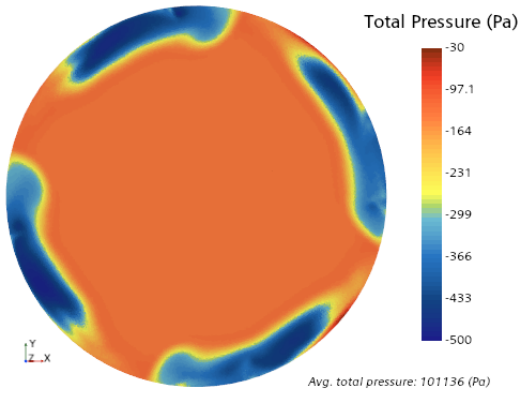

(b) 0.9 m^3/s

Figure 4.4: *AIP* total pressure for case B

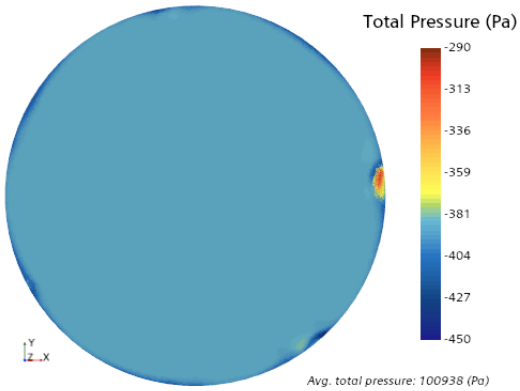

(a) 0.6 m^3/s

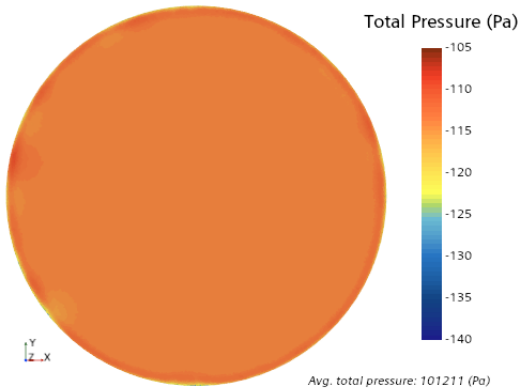

(b) 0.9 m^3/s

Figure 4.5: *AIP* total pressure for case C

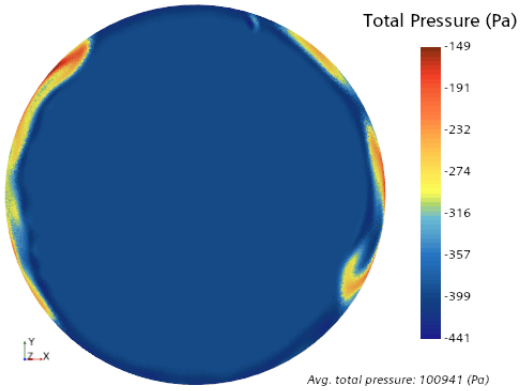

(a) 0.6 m^3/s

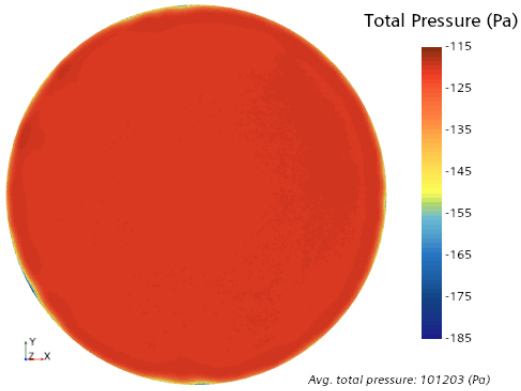

(b) 0.9 m^3/s

Figure 4.6: AIP total pressure for case D

Moreover, there is no clear direct correlation between *CDI* and total sound power. Figure 4.7 illustrates the comparison between the *CDI* and the total sound power output, showing that the relationship between these two variables is not straightforward.

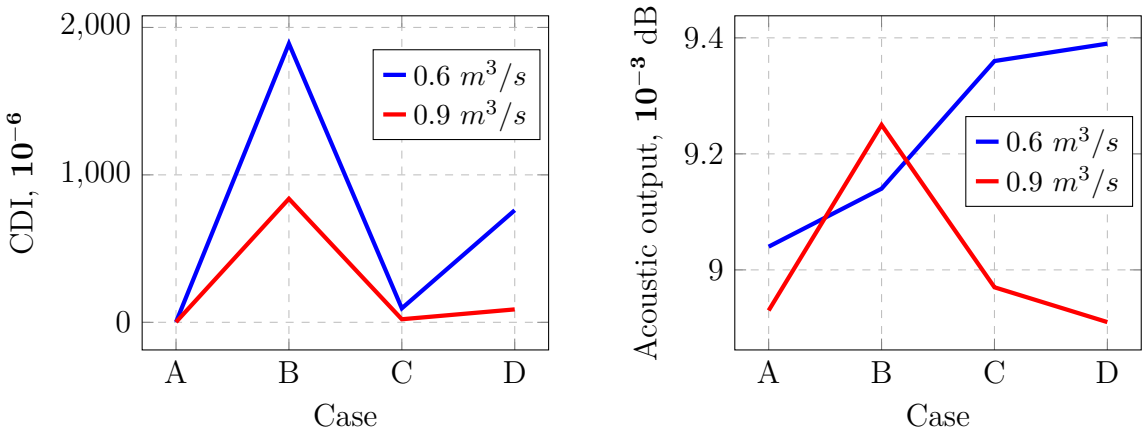

Figure 4.7: Comparison between *CDI* and total sound power

4.4 Obstruction study

Following the acoustic study, a case study was conducted using a half-moon obstruction designed to block half of the inlet area. This study utilized the setup from case D, but with a cylindrical duct that was twice as long as the one used in the acoustic study, and was performed at the operating point of 0.6 m^3/s. The longer duct resulted in a slight increase in both pressure rise and *CDI*, aligning with the trend observed in the acoustic study. Table 4.4 provides a comparison of these results for the same operating point.

Parameter	**Case D for acoustic study**	**Case D for obstruction study**
Pressure rise, Pa	389.29	389.77
CDI, 10^{-6}	760	753

Table 4.4: Comparison of Case D results between acoustic and obstruction study

The obstruction was positioned at five different locations along the duct, with a 4 cm spacing between each subsequent position. The figure below shows the different positions for the obstruction. For ease of reference, the positions are named from A-E with position A being the furthest from the *AIP* while position E being the closest from the*AIP*. For the study, pressure rise was obtained from the simulations and *CDI* was calculated using the data from the simulation. Table 4.5 shows the results of the study.

Position	Pressure rise, Pa	CDI, 10^{-6}
No obstruction	389.77	753
A	172.01	1390
B	112.86	2120
C	93.72	2210
D	2.45	4640
E	-90.84	1970

Table 4.5: Results for obstruction study

Pressure rise

From table 4.5, it can be seen that as the obstruction is placed closer to the *AIP* i.e, from the case with no obstruction to that with the obstruction placed at position E, the rise in pressure decreases and becomes negative that is the flow is reversed for the obstruction at position E. This is shown in the graph in figure 4.8.

Figure 4.8: Pressure rise vs. obstruction position

The reason for this is that the obstruction causes flow distortion, creating areas of turbulence and separation upstream of the fan. These turbulent and separated flows result in uneven loading of the fan blades, reducing their efficiency and the overall pressure rise that the fan can generate. Additionally, the obstruction increases dynamic losses by causing more drag and resistance within the flow. As a result, more of the airflow's energy is dissipated as heat rather than being converted into pressure, further reducing the fan's ability to generate a positive pressure rise. Figure 4.9 shows how the obstruction causes flow distortion upstream of the fan.

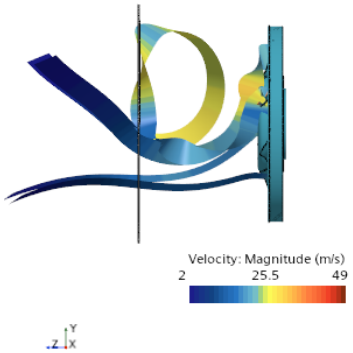

Side view

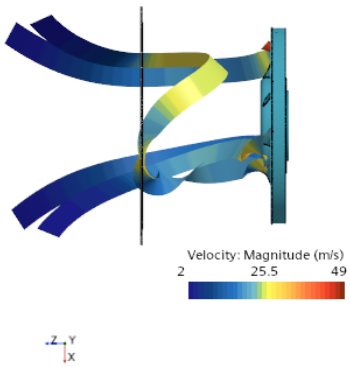

Top view

(a) Position A

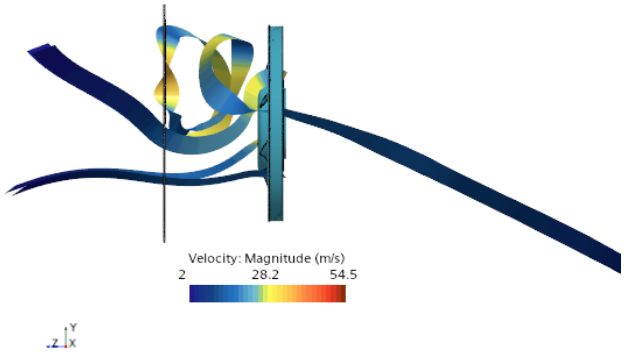

Side view

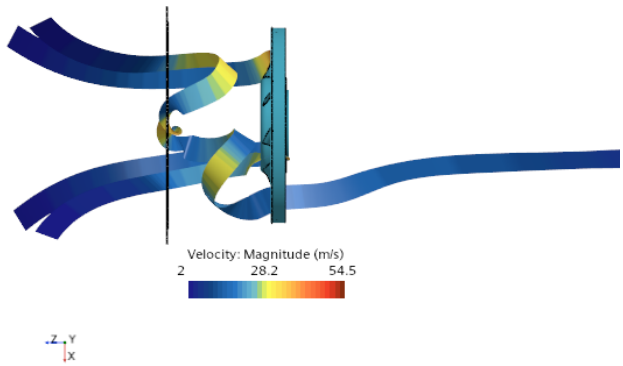

Top view

(b) Position B

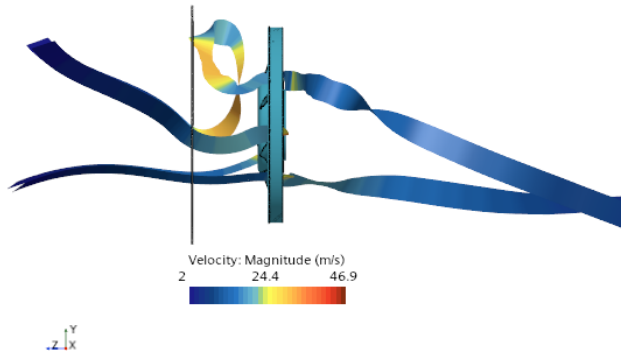

Side view

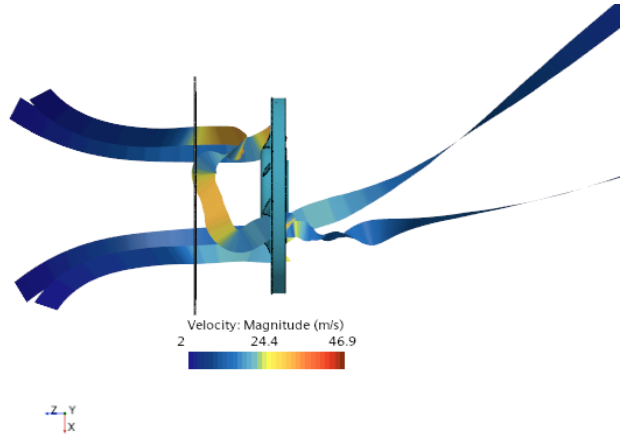

Top view

(c) Position C

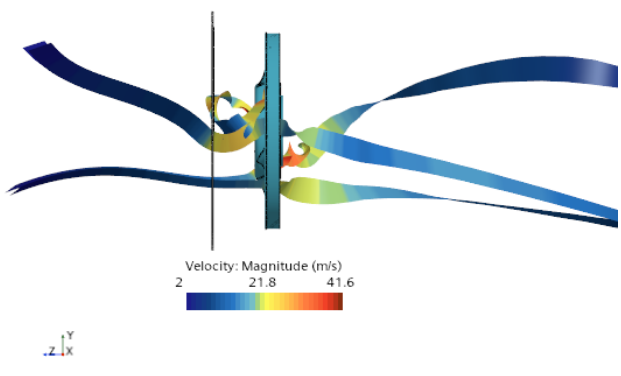

Side view

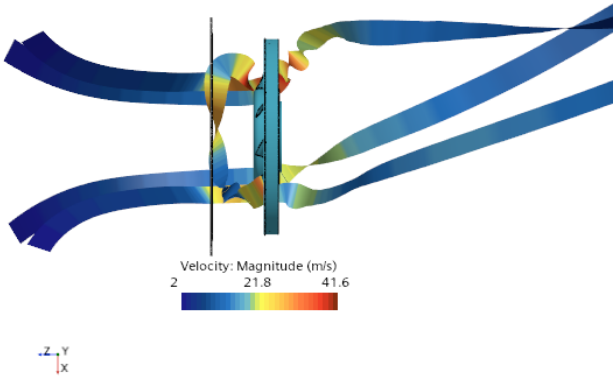

Top view

(d) Position D

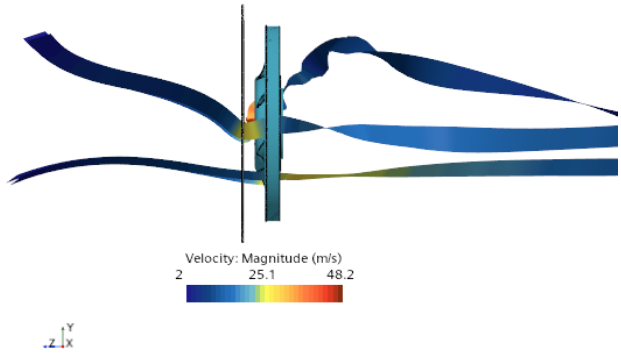

Side view

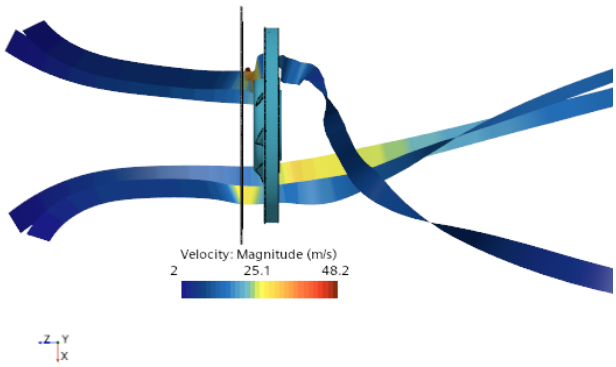

Top view

(e) Position E

Figure 4.9: Streamline view

Circumferential Distortion Index

Table 4.5 indicates that the *CDI* increases progressively as the obstruction moves closer to the fan, with the highest values observed near the *AIP*. However, at position E, although the distortion decreases slightly compared to position D, it remains higher than at position A, where the obstruction is furthest from the *AIP*. This trend is visually represented in Figure 4.10, highlighting how proximity to the fan generally intensifies the circumferential distortion, with a notable, though limited, reduction at the closest position. The reason for this could be that the *AIP* is slightly upstream of the fan which makes it even closer to the obstruction at position E so the effect of distortion is not captured.

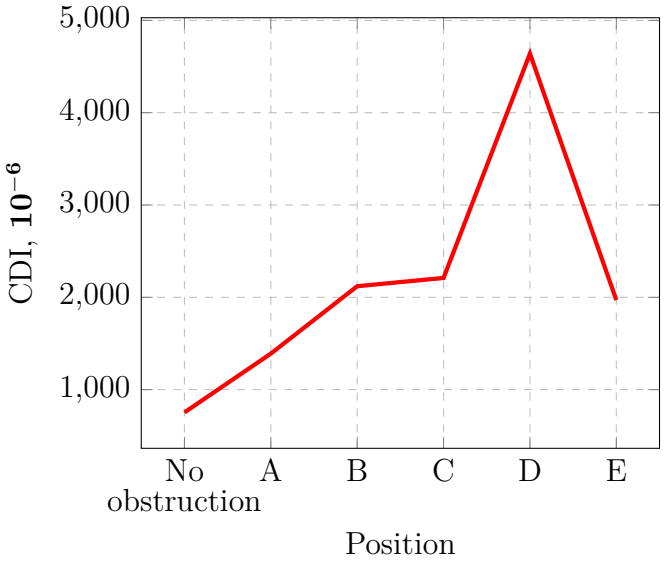

Figure 4.10: *CDI* vs. obstruction position

The total pressure contours for the *AIP*, as shown in the figure 4.10, illustrate how the distortion evolves from position A to position E. It is evident that at position E, there is almost no distortion, as discussed previously.

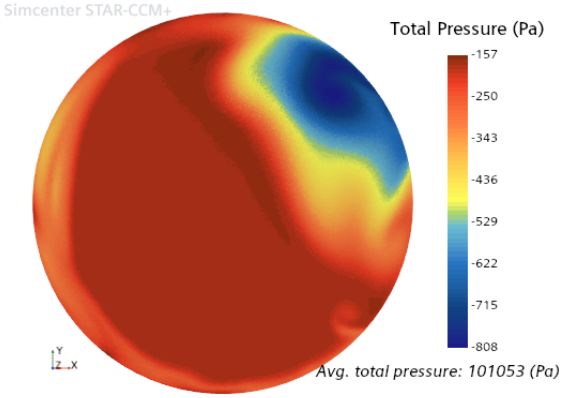

(a) Position A

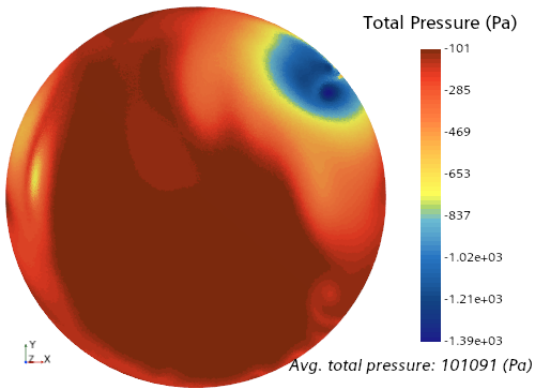

(b) Position B

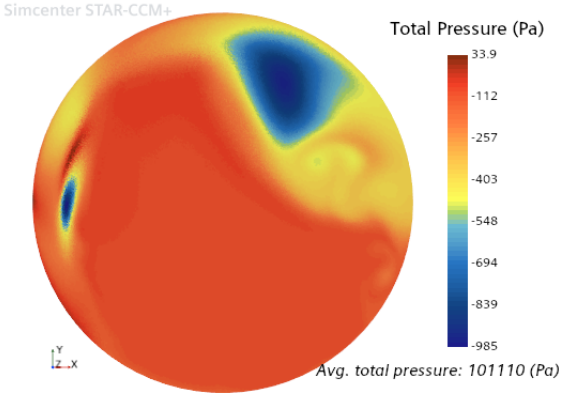

(c) Position C

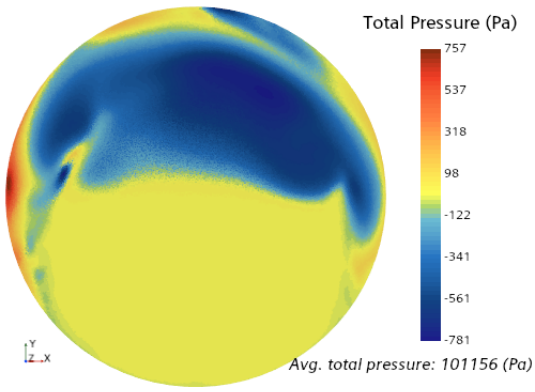

(d) Position D

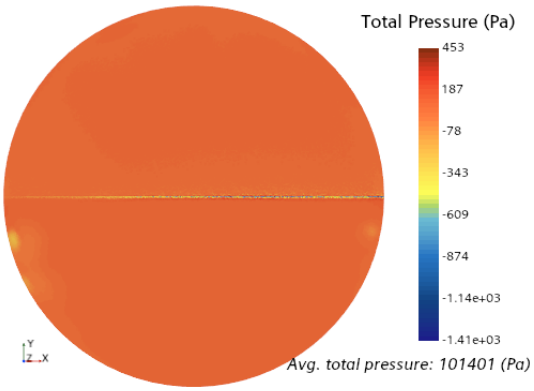

(e) Position E

Figure 4.10: *AIP* total pressure for different obstruction positions

5
Conclusion

This thesis explored the aerodynamic and acoustic performance of electric fans used in automotive cooling systems, with a focus on installation configurations such as cylindrical ducts and bell-mouths. Computational approaches were employed to assess the impact of these configurations on fan efficiency, pressure rise, and acoustic output.

The study found that certain configurations, particularly the addition of bell-mouths, resulted in improved flow uniformity and reduced circumferential distortion. This contributed to an overall increase in pressure rise and a more stable airflow, which is crucial for maintaining the performance of thermal management systems in electric vehicles. However, the relationship between installation effects and acoustic output was less straightforward. While some configurations reduced noise levels, others showed increased acoustic output, indicating a complex interaction between the fan's geometry and the airflow.

Additionally, the obstruction study highlighted the negative impact of partial blockages on fan performance. As the obstruction moved closer to the fan, the pressure rise decreased, eventually leading to flow reversal, while the circumferential distortion index (CDI) increased. This study underscores the importance of carefully considering the placement and design of fan inlet components to minimize performance losses and noise generation.

However, while some trends were identified, establishing a definitive correlation between the pressure rise, distortion indices, and acoustic output remains challenging. More experimental data is needed to strengthen these findings, particularly in varied configurations and operating conditions. Additionally, aeroacoustic simulations could provide deeper insights into the complex interactions between airflow dynamics and noise generation. These further investigations would be crucial for more accurately predicting the acoustic behavior of fan systems and refining designs to reduce noise without compromising performance.

In conclusion, the findings of this thesis provide valuable insights into the design and optimization of fan systems for future electric vehicles. By improving fan performance and reducing acoustic output, these advancements can help meet the stricter noise regulations and thermal management requirements of modern vehicles. Future research could further investigate the correlation between pressure rise and acoustic behavior, as well as explore additional geometric modifications to enhance both

aerodynamic and acoustic efficiency.

Bibliography

[1] Frank M White, CO Ng, and S Saimek. *Fluid mechanics*. McGraw-Hill, cop., 2011.

[2] Siemens. STAR CCM+ User Manual. Wall treatment. Accessible with a STAR-CCM+ license.

[3] Filip Milikic. "Simulation on centrifugal fans operating at close distance: An investigation of different air handling unit constructions to improve fan efficiency". In: (2021).

[4] Johan. *How to setup Rigid Body Motion (RBM) and Moving Reference Frame (MRF) in simulations Simcenter Star-CCM+*. Last accessed on 9th July 2024. 2022. URL: https://volupe.com/simcenter-star-ccm/how-to-setup-rigid-body-motion-rbm-and-moving-reference-frame-mrf-simulations-in-simcenter-star-ccm/.

[5] Florian J Krömer. *Sound emission of low-pressure axial fans under distorted inflow conditions*. FAU University Press, 2018.

[6] Peter Davidson. *Turbulence: an introduction for scientists and engineers*. Oxford university press, 2015.

[7] COMSOL. *The Spallart-Allamras Turbulence Model*. Last accessed on 2nd August 2024. URL: https://doc.comsol.com/5.5/doc/com.comsol.help.cfd/cfd_ug_fluidflow_single.06.093.html.

[8] Jiří Pečinka et al. "Jet engine inlet distortion screen and descriptor evaluation". In: *Acta Polytechnica* 57.1 (2017), pp. 22–31.

DEPARTMENT OF SOME SUBJECT OR TECHNOLOGY
CHALMERS UNIVERSITY OF TECHNOLOGY
Goteborg, Sweden
www.chalmers.se

CHALMERS
UNIVERSITY OF TECHNOLOGY